High irreversibility fields and current densities in $NdBa_2Cu_3O_{7-\delta}$ single crystals and melt-textured samples

Th. Wolf, A-C. Bornarel, H. Küpfer, R. Meier-Hirmer, and B. Obst
Forschungszentrum Karlsruhe, Institut für Technische Physik,
and Universität Karlsruhe, Postfach 3640, D-76021 Karlsruhe, Germany
(Received 31 March 1997)

$NdBa_2Cu_3O_{7-\delta}$ single crystals and melt-textured samples were prepared in reduced atmospheres starting from the Nd-poor side of the phase diagram in order to minimize the Nd/Ba substitution and the second phase content. Current density j and irreversibility field B_{irr} were measured as a function of temperature and angle between the c axis and applied field direction in samples with different impurity and oxygen contents. Current density vs field shows a pronounced peak effect which results from small clusters of oxygen vacancies, whereas a second peak is related to the twin structure. The current density at 77 K is for fields up to 4 T above 4×10^4 A/cm^2 and reaches values of 1.2×10^5 A/cm^2 in the peak at 2.1 T. The irreversibility fields parallel to the c axis reach 13.4 and 11.8 T at 77 K in pure and homogeneous single crystals and melt-textured samples, respectively. These extremely high values, which are caused by the twin structure, decrease to 10 and 8 T, respectively, if the current is optimized. The correlation and interference between j and B_{irr} in the presence of weakly and strongly interacting defects such as small clusters of oxygen vacancies and Nd-422 precipitates, respectively, as well as the influence of the twin structure are analyzed and discussed.
[S0163-1829(97)01134-X]

I. INTRODUCTION

Technical application of high-temperature superconductors requires high critical currents and high irreversibility fields at 77 K. The best candidate up to now to have this potential for bulk material is the $YBa_2Cu_3O_y$ system (Y-123), where by the introduction of finely dispersed Y_2BaCuO_5 particles (Y-211) into the Y-123 matrix an increased pinning at low fields leading to critical currents up to 10^5 A/cm^2 could be achieved.[1,2] Each type of pinning center, for example, Y-211 inclusions, point defects, defect clusters, etc., has its own signature in the j versus H dependence, and it depends crucially on the relative concentrations of all these defects whether a sample is able to carry a large current or not. Large Y-211 inclusions increase the current at low fields only and diminish the influence of the other important pinning centers. Therefore, if one tries to improve the current density in the field range from 1 to 5 T, for example, for the application of Y-123 in magnetic bearings, one has to reduce the Y-211 inclusions to a tolerable low content. This is only possible if we do not apply the usual melt texture process, where Y_2O_3 or Y-211 is added to the Y-123 phase. Instead of doing this, one has to start from pure Y-123 or Y-123+Cu/Ba mixtures. This significantly decreases the amount of Y-211 phase in the superconductor but can now lead to an increase of the critical current at medium fields. In 1994, Yoo *et al.*[3] showed that by processing Nd-123 in a low-pressure oxygen atmosphere, melt-textured samples with high irreversibility fields, with a T_c value of 96 K and with high critical currents in a pronounced peak could be obtained. This peak effect was attributed to the substitution of Nd ions onto the Ba site which should act as a pinning center. Recently, we have shown that even irreversibility fields as high as 13.4 T at 77 K can be found in Nd-123 single crystals.[4] Although we could show that the peak is due to oxygen vacancy clusters and not to Nd/Ba defects we are convinced that Nd-123 bulk superconductors have a larger potential for technical applications than the Y-123 system. The following paragraphs will give a review of the differences between the members of the R-123 family.

It is well known that most of the rare-earth elements can replace Y in the Y-123 structure and form a stable compound with T_c values around 90 K. At first glance the whole series looks very similar but there are important differences between these compounds which increase with the difference between the rare-earth ionic radii. That the peritectic melting temperature (T_{perit}) increases with increasing ionic radius is well known. In air T_{perit} is near 1015 °C for Y-123, and near 1080 °C for Nd-123. This high stability of Nd-123 is also reflected in the higher growth velocity of Nd-123 crystals as compared to Y-123 crystals.[5] Fundamental differences can be found in the phase diagrams. Small sized ions such as Y form stoichiometric Y-123 and Y-211 (green phase) compounds, maybe even down to a level of 1000 ppm, whereas large sized ions such as Nd form a Nd-422 (brown phase) and a Nd-123 compound where a significant amount of Ba can be replaced by Nd. In 1987 a nominal formula $R_{1+x}Ba_{2-x}Cu_3O_y$ was given by Takekawa *et al.*,[6] which takes as a basis that only the R ion replaces the Ba ion and not the other way around. Recent results show that at least in Nd-123 one has to accept a Ba population at the Nd site.[7] Such a homogeneity range, in principle, is a four-dimensional space which depends on temperature, oxygen partial pressure, and the cations which are in equilibrium with the 123 phase. At 950 °C in air Gd-123 can exhibit an occupation of Gd on the Ba site of up to $x=0.20$, and in La-123 x can increase up to 0.70. These homogeneity ranges decrease with increasing temperature and with decreasing oxygen partial pressure.[8,9,10,11] Today one relies on a model where x shrinks to zero at appropriate O_2 pressures and tem-

peratures, but this seems to be oversimplified if we look into details.[12] To be sure to prepare a stoichiometric Y-123 phase, or a Nd-123 phase with a desired x value, one has to avoid Y-123+Y-211 or Nd-123+Nd-422 mixtures and start with R poor mixtures with adjusted cation ratios. This greatly effects the usual melt texture process, where Y-123+Y-211 mixtures always lead to the largest x value. In addition one has to say that the peritectic decomposition of Y-211 to form Y-123 is a very unusual one, and we cannot expect that it develops in the same way for other R-211 compounds, especially for the Nd system where R-211 does not exist at all.

After the sample preparation the 123 phase has to be oxidized to exhibit good superconducting properties. In Y-123 the relevant oxidation isotherms are published many times as a function of temperature and oxygen partial pressure. Again, these isotherms cannot be used for other R-123 systems because each compound needs its own special oxidation treatment. In general, it can be said that R-123 with a larger R ionic radius needs a lower oxidation temperature or a higher oxygen pressure compared to a small size R ion to establish the same oxygen content in 123. Furthermore, the T_c versus O_y curves are different for different R-123 compounds. For Y-123 we know that there is a maximum T_c value of 93 K at the composition $O_{6.93}$.[13] If we want to compare these maximum T_c values of different systems we first have to look for the correct oxygen content where this maximum appears. Again there is a trend with the R ionic radius. Small R-123 compounds exhibit a T_c maximum below $O_{6.90}$, whereas T_c of Nd-123 is highest at $O_{7.0}$, and La-123 at a hypothetical composition of $O_{>7.0}$. These maximal T_c values now exhibit a trend with the ionic radius from $T_c=87$ K for Yb-123 to $T_c=96$ K for Nd-123 to an extrapolated T_c value of 98 K for La-123.[14,15] While these high T_c values of R-123 with large R ionic radii are desired, any occupation of R on the Ba site in these compounds will lead to a T_c reduction. In the following section all these trends have been considered to prepare stoichiometric pure as well as doped Nd-123 single crystals and melt-textured samples.

II. EXPERIMENT

A. Crystal growth

Nd-123 single crystals have been grown from BaO/CuO fluxes by the slow cooling method.[16] Calcination of the high-pure (5 N) Nd_2O_3, $BaCO_3$, and CuO powder mixtures took place in an Y-stabilized ZrO_2 crucible in an air-tight chamber furnace at 1010 to 1030 °C. The furnace atmosphere was 50 mbar air/950 mbar Ar. After a complete melt was formed, the furnace was slowly cooled down to start the crystal growth process. Between 950–960 °C which was the end of the cooling ramp the remaining liquid flux was decanted within the furnace to separate the crystals from the flux. After cooling down to room temperature selected crystals were further annealed in a tubular furnace under flowing oxygen of 1 bar. This process between 600–380 °C took about 800 h. A second oxidation treatment in the range 480–280 °C and 175 bar oxygen which took about another 300 h followed. The crystals were measured in this highly oxidized state and after various reduction steps in 1 bar oxygen in the temperature range 310–430 °C. The oxygen content of each state was obtained using the isotherms of Kishio *et al.*[17] Although these data may not be exact concerning the absolute oxygen compositions, differences within one sample can be estimated with a higher accuracy. This is for two reasons: first, the isotherms are believed to depend on the Nd/Ba ratio of the Nd-123 phase. The actual Nd/Ba ratio of the reported isotherms is unknown. Second, there are hints that annealing the crystals in the range 310–430 °C for 3 days is not long enough to establish the equilibrium oxygen content. Therefore, the oxygen content after the reduction steps could be underestimated.

B. Melt texture

For the preparation of melt-textured Nd-123 pseudocrystals we used either pure, vacuum-synthesized Nd-123 powders (TA series in Table II), Nd-123+5% CuO+5% BaO mixtures (TB and TD series in Table II), or Nd-123+5% CuO+4% BaO, 1% SrO mixtures (TC1, Table II). After milling the powders were pressed uniaxially with 3 torr 30 sec to form green pellets with a diameter of 15 mm and thicknesses between 1 and 5 mm. The texture process took place in an atmosphere of 80 mbar air and 920 mbar Ar. After a fast heating to 1050 °C and a holding time of 0.5 h, the pellets were fast cooled to 1030–1020 °C and then at rates between 1.3 to 1.5 °C/h to about 900 °C where the furnace was shut off. Oxygen annealing was performed in 1 bar flowing oxygen or in a static oxygen atmosphere of up to 400 bar, similar to the treatments of the single crystals. The oxygen contents of the samples were determined from Kishio's isotherms.[17]

C. Sample characterization

Oxidized single crystals with sizes of up to $4\times4\times4$ mm^3 were examined with a polarized light microscope. The twin structure as well as the color of the domains confirmed the high orthorhombicity and hence the high oxygen content of the crystals. Heat treatments and the process of oxidation often have introduced planar cracks parallel to the ab plane, especially in crystals with thicknesses above 1 mm. This degradation process can be reduced by using slower cooling rates and by avoiding steep oxygen gradients within the samples. Crack-free crystals were selected and their c axes were determined from the twin pattern.

Melt-textured pellets usually contained several grains with volumes between 1 and 50 mm^3. The grains were cleft, then oriented using a microscope and, finally, cut into rectangular shapes by a wire saw. X-ray diffraction measurements for the analysis of the second phase contents of the textured samples were carried out with a STOE two-circle powder diffractometer using Cu $K\alpha_1$. The impurity content of the samples was measured using energy dispersive x-ray analysis (EDX).

D. Superconducting characterization

The magnetic moment m of the crystals and the melt-textured samples due to an induced shielding current was measured with two vibrating sample magnetometers (Oxford Instruments), one of them being equipped with a rotatable sample holder. Measurements were made as a function of

applied magnetic field B, temperature T and angle ϕ between the B direction and the c axis of the samples at a constant sweep rate dB/dt of 10^{-2} T/s. This value is related to an electric field E at the surface of the samples between 10^{-2} and 10^{-1} μV/cm. For $B\|c$, which corresponds to $\phi = 0°$, the current density j within the a,b plane was determined from the hysteresis width Δm, which is the difference of m between increasing and decreasing B using the extended Bean model. The measured moment is as usually the component m_p parallel to B. In some measurements the orthogonal component m_0 was also investigated in addition. This allows us to construct the vector of the magnetic moment m. The angular-dependent measurements were used in order to investigate the influence of the anisotropy and of the correlated and uncorrelated crystal defects on the irreversible superconducting properties. This requires the recognition or elimination of the geometrical influence of turning a superconducting platelike specimen in an applied field.[18] For this reason we used polycrystalline $PbMo_6S_8$ samples with the same geometrical shape as our investigated Nd-123 specimens.

The melt-textured pellets were cut in such a way that no grain boundaries were within the investigated parts. Intragrain granularity in the single crystals and melt-textured samples were excluded by detecting j as a function of sample size or comparing j from Δm with that value obtained from the magnetic field necessary for remagnetizing. This relates the investigated properties of the irreversible magnetic moment exclusively to flux pinning and the influence of thermal relaxation.

The irreversibility field $B_{\rm irr}$ as a function of T and ϕ was also determined from magnetization measurements. The E criteria was the same as for the determination of j. The current criteria was $100\,A/\mathrm{cm}^2$ or alternatively—if the current peak is well pronounced—1% of the j value at the peak was chosen. In the latter case $B_{\rm irr}$ in the temperature region above 90 K becomes more reliable. Thus, the discussed $B_{\rm irr}(T,\phi)$ value corresponds to a resistivity between about 10^{-4} and 10^{-3} $\mu\Omega$ cm, related to a current-voltage characteristics with an exponent n between 2 and 4 for a power-law approximation $E \sim j^n$. Theoretical predictions for the transition of the vortex lattice from the solid into the liquid state are settled in just this region of $E(j)$ characteristics.

In one single crystal the upper critical field B_{c2} was obtained from measurements of the reversible magnetic moment versus T at a constant applied field. The value was estimated from the crossing point extrapolating $m_{\rm rev}$ linearly from the normal state and from the superconducting state. The normalized relaxation rates were obtained from Δm measured with various sweep rates $S = d(\ln \Delta m)/d(\ln dB/dt)$. The superconducting transition temperature T_c was determined from the midpoint of the diamagnetic signal at 5×10^{-4} T.

III. RESULTS AND DISCUSSION

X-ray diffraction analysis of powders of melt-textured samples resulted in nearly single phase spectra. The only secondary phase which could be detected was $Nd_4Ba_2Cu_2O_{10}$(Nd-422). For the TC and TB samples we estimated a Nd-422 phase content of $<10\%$, and for TA even less than 5%. Determination of the impurity content of the samples by EDX was carried out only on single crystals. For melt-textured samples we expect the same purity in the processed samples as in the high-pure starting materials. Single crystals, however, can take up Y and Al which are present in the ZrO_2 crucibles, and which can be set free during crystal growth due to crucible corrosion. With the exception of Y all other impurity elements, especially Al and Sr, were found to be below the detection limits of EDX. As Y only substitutes for Nd, a site occupation of $(5\pm1.3)\%$ Y was estimated. Within this resolution we could not detect any difference between the XA and XB crystals. Anyway, by comparison of the two growth procedures we expect a slightly smaller Y content being present in the XA crystals as a consequence of the reduced crucible corrosion during their growth.

TABLE I. Oxygen deficiency δ, transition temperature T_c, irreversibility field $B_{\rm irr}$, and current density j_p at the maximum field B_p both at 77 K for the Nd-123 crystals XA and XB. Numbers 1 and 7 represent the crystal after high-pressure oxidation.

Sample	δ	T_c(K)	$B_{\rm irr}(T)$	j_p (10^4 A/cm^2)
XA1	<0.04	94.6	13.4	2.7
XA2	0.05	94.6	13.0	3.5
XA3	0.06	94.7	11.9	4.7
XA4	0.08	94.3	11.1	6.2
XA5	0.09	93.9	9.8	8.3
XA6	0.11	93.3	7.8	7.8
XA7	<0.04	94.8	12.1	2.7
XB1	<0.04	93.8	10.1	5.1
XB2	0.08	93.1	7.0	12.7
XB3	0.09	91.8	4.6	11.5

Current densities and irreversibility fields are discussed by two representative single crystals XA and XB, as well as by three melt-textured samples TA, TB, and TC. Table I gives some characteristic properties of both crystals in different oxidation states related to the numbers. High-pressure oxidation with $\delta<0.04$ corresponds to number 1 and 7. The irreversibility field $B_{\rm irr}$ and the current density j_p are measured at 77 K with the field parallel to the c axis of the crystal. The current density is the value at the field B_p at which the current has a maximum. Table II gives the properties of the melt-textured samples. As in Table I, high-pressure oxidation is related to number 1, whereas number 2 and 3 correspond to subsequent oxygen reduction.

A. Critical currents in single crystals

The defect structure which determines the irreversible properties such as $j(B,T,E,\phi)$ and $B_{\rm irr}(T,E,\phi)$ can be divided into correlated and uncorrelated pinning centers. Twins and CuO_2 planes belong to the correlated structure which are relevant within their characteristic trapping angles around $B\|c$ and $B\|a$, b, respectively.[19] In this investigation we shall not discuss intrinsic pinning from CuO_2 planes and focus on to the twin structure which is important for the

TABLE II. Oxygen deficiency δ, transition temperature T_c, irreversibility field B_{irr}, and current density j_p at the maximum field B_p both at 77 K for the Nd-123 melt-textured specimens TA, TB, TC, and TD. Number 1 represents the specimens after high-pressure oxidation.

Sample	δ	T_c(K)	$B_{irr}(T)$	j_p (10^4 A/cm^2)
TA1	<0.04	95.5	9.2	1.4
TA2	0.05	94.0	7.6	2.4
TA3	0.09	90.6	3.8	1.6
TB1	<0.04	95.3	8.8	3.5
TB2	0.05	95.0	7.7	5.8
TB3	0.09	90.1	2.9	3.2
TC1	<0.04	93.2	6.7	6.5
TD1	<0.04	94.6	11.8	0.4

usual geometry current within the a,b plane and $B\|c$. The influence of the twin structure depends on the mean twin spacing, the formation of the twin complexes, and the integrity of the twin walls. The uncorrelated structure consists of point defects and small clusters or agglomerates which may result from diffusion or phase separations. Point defects such as oxygen vacancies, for instance, are not important for the pinning behavior above 50 K because the interaction potential is smeared out by the thermal oscillation of the vortices. Therefore, pure and fully oxidized crystals show a very low and monotonically decreasing current with B in the higher temperature region.[19] Such twinfree Y-123 crystals were deoxidized, rapidly cooled down and measured. The $j(B)$ dependence shows then a very weak maximum of the current around 4 T (dashed line in Fig. 1). Aging at room temperature, which does not change the oxygen content of the crystal but allows the diffusion of oxygen vacancies, results after about 5 weeks in a very well pronounced peak effect (PE) or fishtail (solid line in Fig. 1).[20] This demonstrates that the prominent PE is not caused by point defects but by small agglomerates, for instance, of oxygen vacancies in agreement with similar observations by Erb *et al.*[21] This is further supported by γ irradiation of crystals which do not exhibit a PE; here the introduced point defects increase the current only below 20 K but do not produce a peak at higher temperatures.

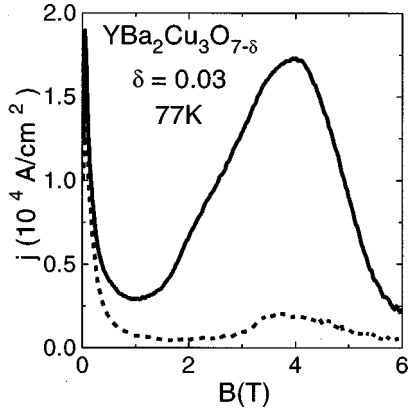

FIG. 1. Current density j vs applied magnetic field B of a twinfree Y-123 crystal before (dashed line) and after (solid line) it was stored at room temperature for 5 weeks.

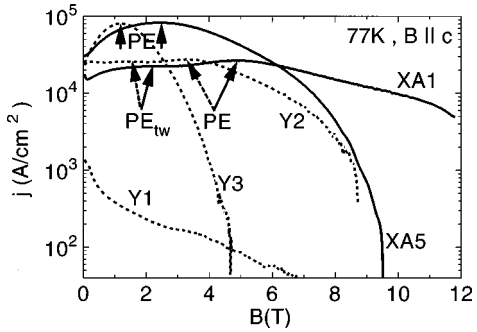

FIG. 2. Current density j vs applied magnetic field B of different Y-123 and one Nd-123 crystal with different oxygen deficiencies (XA1 and XA5). PE indicates the peak or fishtail effect from uncorrelated defects, whereas PE_{tw} is a peak resulting from the twin structure.

Another current peak PE_{tw} may be caused by the twin structure itself. This peak is not related to a matching condition between twin spacing and vortex distance but probably results from a collective pinning of vortices by the twin structure. This uncorrelated interaction of the correlated twins is expected in a region between the irreversibility field and the strong correlated pinning at lower B and T.[22]

Both defect structures, twins and small clusters, which are of importance at higher temperatures, interfere with each other in a very complex manner which depends crucially on their properties and on T, B, and ϕ. This results for twinned crystals in three characteristic $j(B)$ dependencies as shown for Y-123 by the dashed lines in Fig. 2. The crystal Y1 has a negligible concentration of clusters which is not sufficient to form a PE and also the twin wall pinning is small. In Y2 an increasing concentration of point defects, for instance, from oxygen vacancies or other impurities, results in the formation of clusters which causes a PE. This larger number of defects is probably also responsible for less perfect twin walls which changes their pinning properties. The twin spacing with values between 100 and 400 nm (Ref. 23) is very similar in Y1, Y2, and Y3 and is not able to account for the quite different influence of the twin structure between Y1 and Y2. In crystal Y2 both structures are of comparable strength, whereas in Y3 the increasing formation of clusters becomes dominant and only PE is present. The solid line of XA1 represents the equivalent Nd-123 crystal to Y2; XA5 corresponds to Y3. A Nd-123 crystal equivalent to Y1 has not yet been prepared because the impurity content or the degree of Nd/Ba substitution of our samples is still too high. In the following we discuss the double peak structure of XA1, also observed in Refs. 24, 25, and 26, which is the starting point for optimizing the current in single crystals and melt-textured Nd-123. The investigation of the double peak structure as a function of T, ϕ, and δ supports that PE_{tw} results from the twin structure and PE from the weakly interacting small defect clusters. The very similar dependences of the current on all parameters in Y2 and XA1 excludes an origin exclusively present in Nd-123.[20]

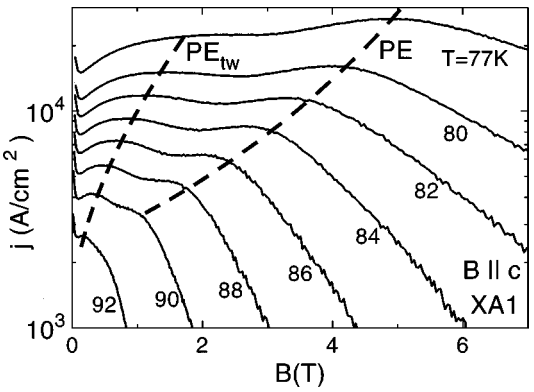

FIG. 3. Peak effect from uncorrelated defects (PE) and from the twin structure (PE_{tw}) in Nd-123 crystal XA1 at different temperatures.

With higher temperatures the interaction between vortices and twin structure decreases less in comparison to the interaction with the isotropic defect structure. This results from the dimensional reduction of the thermal oscillation of the vortices in the presence of correlated defects.[22] The experimental observation shown in Fig. 3 is in agreement with this expectation. The peak from the twins PE_{tw} becomes dominating, whereas PE vanishes between 77 and 90 K. This measurement demonstrates also that PE_{tw} is not a matching peak because its field position decreases with higher T, as is always observed for PE. Further the field which corresponds to the twin spacing is below 0.1 T, much smaller than the peak fields (Fig. 3).

An additional support for the different natures of the two peaks comes from the dependence of Δm on the angle ϕ between c axis and applied magnetic field. In order to get all of the information about the angular dependence of the magnetic moment, the Δm values given in Figs. 4(a) and 4(b) are calculated from the vector of the moment. The inset of Fig. 4(a) demonstrates that PE_{tw} vanishes outside the trapping angle of the twin structure which is about 20°, whereas PE is present in the whole angular regime. The complex angular dependence of PE is related to the angular dependence of B_{irr} discussed later and within the trapping angle to the influence of the twin structure. The influence of the platelike shape on the **m** vs ϕ behavior is negligible up to about 60°. This was proved by measuring $\mathbf{m}(\phi)$ of a polycrystalline $PbMo_6S_8$ sample of the same shape as the Nd-123 single crystal [solid diamond in Fig. 4(a)]. In the angular regime of about $\pm 20°$ around $B \| c$, Δm is increased by twin wall pinning in the whole field range [Fig. 4(a)]. At 1.5 T the pronounced maximum at $\phi = 0°$ from PE_{tw} is also shown in Fig. 4(a). Within the trapping angle the PE is roughly added to this twin wall pinning. Therefore the real strength of PE can only be estimated for $\phi > 20°$ [inset of Fig. 4(a)]. This increase from twin wall pinning is expected for a Lorentz force directed perpendicular to the twin walls. The closed current loops of the magnetization measurements always have, besides a Lorentz force perpendicular to the twin walls, a corresponding parallel component. The pinning force against movement of vortices parallel to the twin walls is expected to be much smaller than the one perpendicular to them. If the pinning force between vortices and clusters exceeds this weak longitudinal twin wall interaction, the force of the vortex lattice

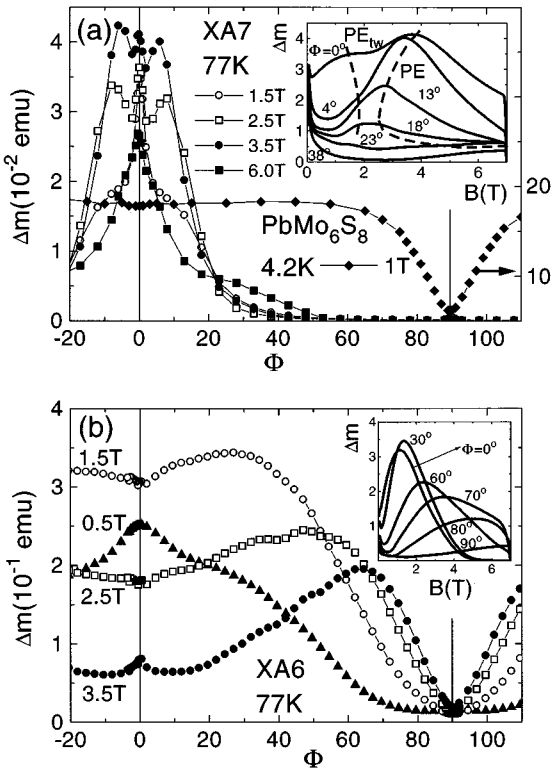

FIG. 4. Hysteresis width Δm from the vector of the magnetic moment vs angle Φ between applied magnetic field B and the c axis at different B values for the same Nd-123 crystal after high-pressure oxydation XA7 (a) and after oxygen reduction XA6 (b). The inset in (a) shows the peaks in XA7 from uncorrelated (PE) and correlated defects (PE_{tw}), whereas in XA6 PE dominates [inset of (b)]. For comparison $\Delta m(\Phi)$ of a polycrystalline $PbMo_6S_8$ sample of the same geometrical shape as XA6 is also shown. This variation corresponds to the geometrical influence on the angular dependence.

against shearing between vortices within and outside the twin walls may determine the current.[27,28] This shear force is expected to decrease towards $\phi = 0°$ because the length of the vortices parallel to the twin walls becomes maximum at $\phi = 0°$. In the field region where PE has its maximum [2.5 and 3.5 T in Fig. 4(a)] this upper limit of the shear force may be reached at about $\phi = \pm 6°$. Below this angle Δm decreases because the shear interaction becomes the weakest force. The sharp maximum around $B \| c$ is, as discussed above, related to the twin wall pinning of the current flowing parallel to the twin walls. Summarizing, $\Delta m(B, \phi)$ of XA7 results from the isotropic vortex interaction with the clusters (PE) and from the anisotropic interaction with the twin structure. The latter must be divided into components perpendicular and parallel to the twin walls which causes pinning (PE_{tw}) and channeling, respectively. Their ratio depends on the strength and properties of both structures as well as on the orientation of the twin domains with respect to the Lorentz force. The influence of the intrinsic anisotropy and the geometrical shape of the crystal can be neglected within the trapping angle regime.

If the concentration of the uncorrelated structure becomes dominant, the influence of the twins vanishes. The corresponding measurements shown in Fig. 4(b) are made on the same crystal as in Fig. 4(a) but with a larger oxygen defi-

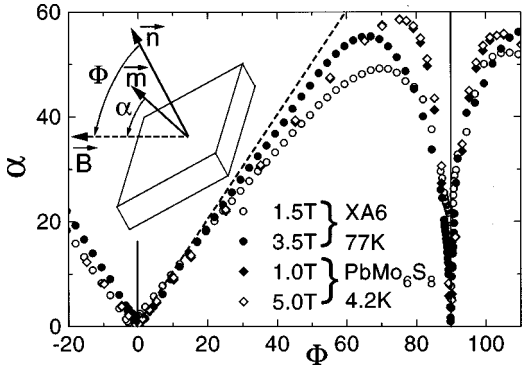

FIG. 5. Angle α between the c axis and magnetic moment **m** vs Φ for the Nd-123 crystal XA6 and a polycrystalline $PbMo_6S_8$ sample of the same geometrical shape as XA6. The dashed line corresponds to $\alpha=\Phi$ at which **m** is parallel to the plate normal **n** or to the c axis of the Nd-123 crystal.

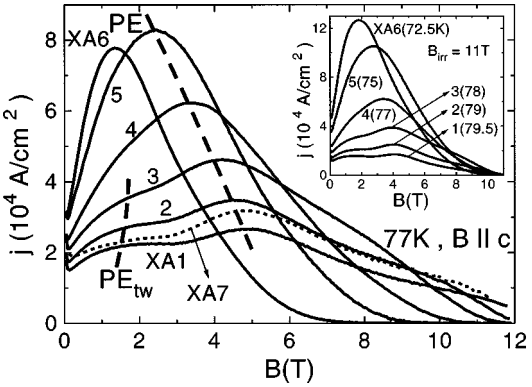

FIG. 6. Development of the current density j vs B as a function of oxygen deficiency in the Nd-123 crystal XA. XA1 and XA7 represent the high-pressure oxydation states with $\delta<0.04$ before and after oxygen reduction, respectively. The inset shows $j(B)$ at different temperatures which all have the same irreversibility field B_{irr} of 11 T.

ciency. The peak from the twins PE_{tw} has vanished and only PE is present in the whole angular regime [inset of Fig. 4(b)]. The residual influences of the twin structure are seen in the increase of Δm below and above the peak [0.5 and 3.5 T in Fig. 4(b)] and in the small decrease from channeling or shearing of vortices in the peak region [1.5 and 2.5 T in Fig. 4(b)]. With the exception of these less pronounced features, $\Delta m(B,\phi)$ in XA6 is determined from $B_{irr}(\phi)$ and the scaling with the field $B_p(\phi)$ at which j has its maximum, and from the platelike geometry of the crystal which governs the direction of the current flow. The last point is demonstrated in Fig. 5 which shows the angle α between the applied field direction and the measured vector of the magnetic moment vs ϕ. For $\alpha=0$ the magnetic moment is directed parallel to the applied field as for $\phi=0°$ and 90°. The measured values are close to the dashed line ($\alpha=\phi$) and indicate that the magnetic moment **m** is almost parallel to the plate normal **n** which corresponds to the c axis of the Nd-123 crystal. This remarkable result, which is the same for the anisotropic single crystals and for the $PbMo_6S_8$ sample, demonstrates that this behavior is not caused by the superconducting anisotropy but by the geometrical shape.[18]

The third confirmation for the different origin of PE and PE_{tw} comes from the dependence of both on the oxygen content. Increasing oxygen deficiency δ makes the uncorrelated defect structure stronger and reduces the influence of the twin structure. Figure 6 shows that PE becomes more pronounced with an increase of δ from XA1 to XA6, whereas PE_{tw} vanishes completely. After the oxygen reduction of $\delta=0.11$ (XA6) the crystal was reoxydized (XA7) below 400 °C 140 bar O_2 and shows a current and irreversibility field behavior very similar to the starting crystal XA1. This reversibility of the structure responsible for PE points to easy diffusion of oxygen vacancies and not to migration of cations leading to Nd/Ba substituted regions or other phase separations.

The increase of δ (Fig. 6) leads to a pronounced PE, a decrease of B_{irr}, and a change of the field dependence of the current; for instance, the ratio B_p/B_{irr} is shifted to much lower values. The maximum current density at B_p of about 8×10^4 A/cm^2 (XA5 in Fig. 6) results from increasing defect concentration accompanied by decreasing pinning energy due to changes of superconducting properties. From XA1 to XA5 T_c is lowered by only 1 K but B_{irr} by about 30% at 77 K. This dramatic drop of B_{irr} is the main reason for the current decreasing again for $\delta>0.09$. Measurements of the current density at temperatures at which B_{irr} is constant, shown for 11 T in the inset of Fig. 6, reveal a clear change of $j(B)$ with δ which points to a larger size of the oxygen depleted regions.

From Fig. 6 it is obvious that a further improvement of j at 77 K is not expected with crystals of such a relatively low impurity content. Other possibilities to raise the current—other than exclusive oxygen reduction—are Nd/Ba, Nd/Y, or Ba/Sr substitutions, other structural defects, or starting with a less pure crystal and then decreasing its oxygen content. The latter process results in considerably higher current densities as shown in Fig. 7, where XB1 and XB2 represent the same crystal but at different oxygen contents which correspond to XA1 and XA4, respectively. The starting crystal XB1 already has, as a result of the higher defect concentration, larger j and lower B_{irr} values in comparison to XA1. This defect structure, present before oxygen reduction, is maintained if δ is increased and causes higher currents at 77 K below 4 T, whereas above, j of XA5 is superior due to

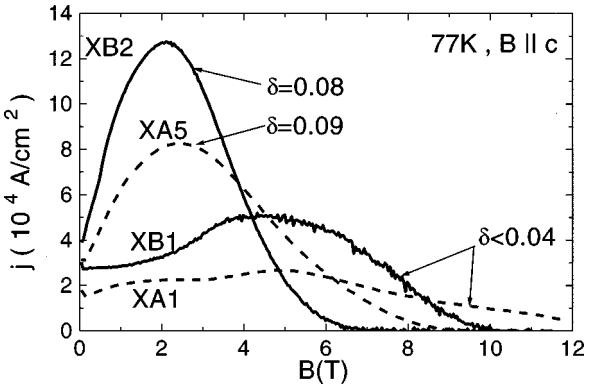

FIG. 7. Current density j vs B in two Nd-123 crystals XA and XB after high-pressure oxydation XA1 and XB1, and after oxygen reduction XA5 and XB2 which results in an optimum current density for each crystal.

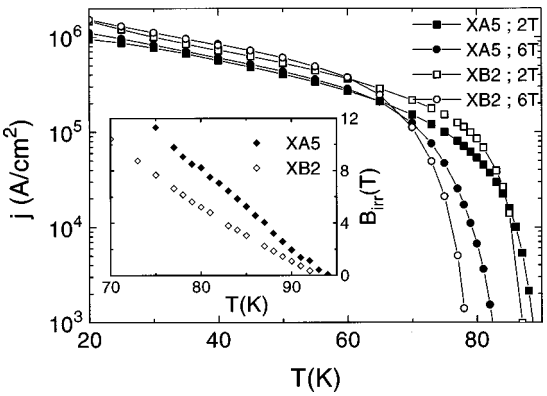

FIG. 8. Current density j vs temperature T in two Nd-123 crystals XA and XB in the peak regions (2 T) and above (6 T). The inset shows the irreversibility field B_{irr} vs T for both crystals.

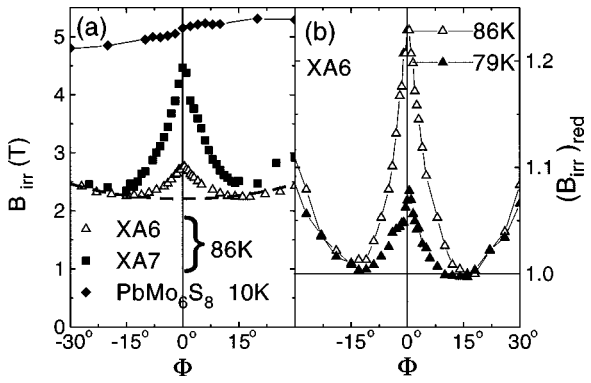

FIG. 9. Irreversibility field B_{irr} vs Φ which is the angle between applied magnetic field B and the c axis for the Nd-123 crystal XA in the oxygen reduced state (XA6) and after subsequent high-pressure oxydation (XA7). For comparison the negligible geometrical influence on $B_{irr}(\Phi)$ of a polycrystalline $PbMo_6S_8$ specimen having the same shape as XA is also shown (a) (b) shows B_{irr} vs ϕ of XA6 measured at 86 and 79 K. Both values are normalized to 1 at the trapping angle of about 15°.

its higher B_{irr}. A comparison of the temperature dependence of j between XA5 and the less pure crystal XB2 in Fig. 8 shows this problem of optimization. The irreversibility field is lower in crystal XB2 due to the larger defect concentration (inset in Fig. 8). As long as B_{irr} has negligible influence on the current at a certain field B, i.e., $B \ll B_{irr}$, the j values of XB2 are higher, which is the case for 6 T only up to 70 K; however, at 2 T this holds up to 86 K. Because $j(B)$ at 77 K is in the region where it is severely influenced from the close neighborhood of B_{irr} an optimization above 1 T always requires a careful consideration of this parameter.

B. Irreversibility fields in single crystals

In pure crystals with a low defect concentration a first-order melting transition is the origin of the crossover from the vortex-solid state into the vortex-liquid state.[29] Disorder from weakly interacting uncorrelated defects smears out the melting transition and transforms it into a second-order vortex-liquid vortex-glass crossover.[30] Both the melting and the vortex-glass transition fields have a minimum at $\phi = 0°$ and increase towards $\phi = 90°$. Correlated defects such as twins transform the melting transition into a Bose-glass transition[31] with a cusplike maximum of $B_{irr}(\phi)$ at $\phi = 0°$.

The melting transition is determined by superconducting properties such as upper critical field, anisotropy, and the Ginzburg-Landau parameter. Oxygen reduction changes these properties and therefore the melting line too. A further influence results from the introduced uncorrelated defects which add static disorder in the vortex lattice to the thermal disorder and in this way lowers the melting point. A correlated structure, however, is expected to raise the transition above the melting line due to the dimensional reduction of thermal disorder. The corresponding increase of B_{irr} from the twin structure depends on the properties of the twins and on the strength of the uncorrelated defect structure. Oxygen reduction or increasing impurity content result in an accumulation of defects in the twin walls and in a minor planarity which destroys the correlation. Secondly, from flux dynamics one expects a decrease of the dimensional reduction with larger static disorder in the vortex lattice. Both influences result in a less pronounced increase of B_{irr} from a correlated structure with increasing strength of the uncorrelated defects. This brief consideration allows one to understand qualitatively the behavior of B_{irr} in the Nd-123 crystals with different oxygen and impurity contents. Figure 9(a) shows the cusplike behavior of B_{irr} at $B \| c (\phi = 0°)$ caused by the twins and, for comparison, B_{irr} of the polycrystalline $PbMo_6S_8$ specimen with the same geometrical shape. The increase of B_{irr} within the trapping angle towards $\phi = 0°$ is about a factor of 2 in crystal XA7 which has the highest oxygen content. Oxygen reduction in XA6 results, as discussed above, in a stronger interacting uncorrelated structure of small clusters and, consequently, the local maximum at $B \| c$ is lowered. With decreasing temperature the cusplike enhancement becomes less pronounced. For instance, $B_{irr}(\phi)$ in XA6 was measured at different temperatures. The enhancement decreases considerably from 86 to 79 K as shown in Fig. 9(b). The largest influence of the twin structure on B_{irr} is expected up to the magnetic field at which the twin spacing matches with the mean vortex distance. The large difference between this field of about 0.1 T and the still remarkable enhancement of B_{irr} at 10 T and above is not understood.

An estimation of B_{irr} at $B \| c$ in the absence of twin structure is indicated by the dashed line in Fig. 9(a). The very similar B_{irr} values for both oxygen contents demonstrate that the influences of the changed superconducting properties, as well as of the added defects on B_{irr}, are negligible within the investigated range of oxygen deficiency. It further proves that the main reason for the difference of B_{irr} between XA6 and XA7 is related to changes of the properties of the twin structure.

Figure 10 shows B_{irr} vs temperature at $\phi = 0°$ for the same crystal in different oxidation states. For the crystals XA1 and XA7 with the highest oxygen content a linear extrapolation, as indicated by the solid line, results in B_{irr} values between 13 and 13.5 T at 77 K. This value is about a factor of 2 larger than usually observed in Y-123 bulk and thin film materials. It is even above the upper critical field of commercial NbTi wire at 4.2 K. It should be mentioned again that these B_{irr} values are measured with very conservative E and j criteria. The lowered irreversibility fields with δ are not caused by the change of T_c but, as discussed above,

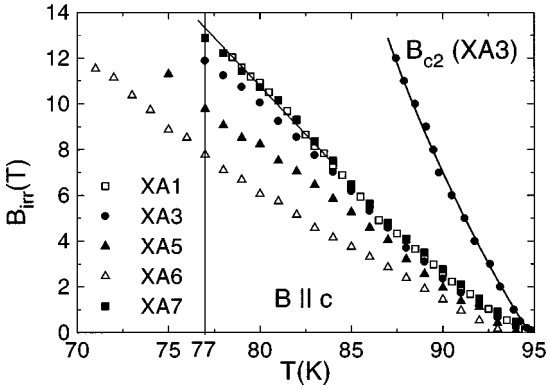

FIG. 10. Irreversibility field B_{irr} vs temperature T in the Nd-123 crystal XA. XA1 and XA7 represent the high-pressure oxydation state with $\delta<0.04$ before and after oxygen reduction, respectively.

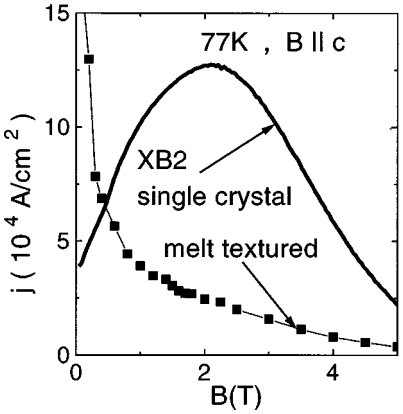

FIG. 11. Current density j vs applied field B for the Nd-123 crystal XB2 with a pronounced peak from uncorrelated weakly interacting defects and for a Y-123 melt-textured specimen with a characteristic $j(B)$ dependence from uncorrelated strongly interacting defects.

by the decreasing influence of the correlated twin structure. A plot of $B_{\mathrm{irr}}\sim(1-T/T_c)^n$ results in n values of about 1.2 which are considerably lower than in Y-123. This points towards a smaller anisotropy and therefore it may be one reason for the higher irreversibility line in Nd-123. The measurement of the upper critical field B_{c2} shows a slope of 1.7 T/K comparable to Y-123 (Fig. 10).

C. Critical currents and irreversibility fields in melt-textured material

The defect structure in melt-textured Nd-123 depends crucially on the preparation path. Generally it can be described by the structure of a single crystal to which larger scale, uncorrelated defects, such as precipitates, holes, or microcracks are added. Therefore in the higher temperature region where point defects are of negligible influence, one has to consider, in melt-textured samples, correlated twins, uncorrelated weakly interacting clusters from impurities or oxygen vacancies, as well as uncorrelated strongly interacting defects. The concentration of the latter is expected to be much smaller than that of the small clusters. This and the quite different interaction strengths are the reason for the dissimilar influences on the irreversible behavior of the vortices. The characteristic field dependence of the current from strongly interacting larger scale defects in a melt-textured sample and from weakly interacting small clusters in a single crystal are demonstrated in Fig. 11. The melt-textured Y-123 contains roughly 20% 211 precipitates and the Nd-123 single crystal XB2 has clusters from impurities and oxygen vacancies. In both samples the twin structure is of negligible influence. It should further be mentioned that the pronounced decrease of $j(B)$ in the melt-textured sample results from the interaction between vortices and defects and is not caused by granularity as checked in Ref. 32. The relatively low concentration of strongly interacting defects increases the current in the low field regime, whereas a much higher concentration of weakly interacting defects produces a PE in the medium field range. The best way to optimize the current would be to increase the concentration of precipitates while simultaneously decreasing their size towards the coherence length. But this can not yet be realized in bulk material which, as a result of the preparation route itself, contains many fewer defects than thin films. Another powerful method is to introduce strongly interacting defects from fast neutron, proton, or heavy-ion *irradiation*. From the relatively low expenditure of preparing samples with currents as shown in Fig. 11, a desirable improvement would be to achieve a simple addition of both currents from a combination of both defect structures. Unfortunately, even this is difficult for two reasons. First, both defect structures cannot be added without interference. For instance, the precipitates may act as defect sinks for impurities or oxygen vacancies preventing the formation of small clusters in their surroundings. Second, even an ideal addition of both defect structures would not result in an addition of the currents because the elementary pinning interaction does not sum up linearly to the global pinning force per volume which determines j. This interference from flux dynamics may suppress the formation of the peak, whereas the current behavior caused by precipitates is not expected to be disturbed by the disorder from the pointlike defects. Therefore, at low fields where the precipitates dominate the pinning interaction, large currents can be easily obtained. On the other hand, achieving a pronounced PE in a melt-textured sample is the much more difficult task. The twin structure and its interference makes an optimization of the current in melt-textured material even more complicated than in single crystals. Large scale defects destroy the regularity of the twin walls and the platelike structure along the c axis results in a misalignment along c. The influence of the twin structure becomes further suppressed by increasing the content of the large scale defects.

Figure 12 shows $j(B)$ for three Nd-123 melt-textured specimens. Sample TC1 is representative of a dominating strongly interacting defect structure with negligible influence of twins. On the other hand, TA1 shows a PE and relatively low currents in the low field region. This $j(B)$ behavior is governed by clusters and twins. These two specimens are characteristic for the two extreme cases. The best compromise up to now between both is represented by TB2 which exhibits current densities above 5×10^4 A/cm^2 up to 3.5 T and an irreversibility field of 8 T at 77 K. Concerning the behavior of the current and the irreversibility field, this specimen is situated between the two others. For reason of

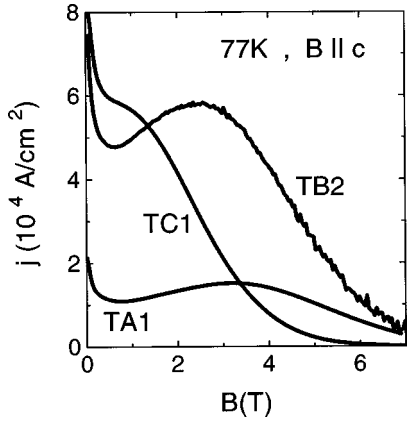

FIG. 12. Current density j vs applied field B for three differently prepared Nd-123 melt-textured samples. The purest sample after high-pressure oxydation TA1 is comparable to XA1, whereas TC1 is the specimen with a higher content of second phases and other impurities. Sample TB2 is somewhere in between both, combining high currents at low B and a peak from weakly interacting defects.

clarity we therefore shall discuss the angular dependences and the influence of the twins on TA1 and TC1.

The $\Delta m(\phi)$ dependence of specimen TA1 [Fig. 13(a)] should be compared with crystal XA7 [Fig. 4(a)]. Both samples are fully oxydized; the relatively low currents of TA1 result from the residual uncorrelated defect structure

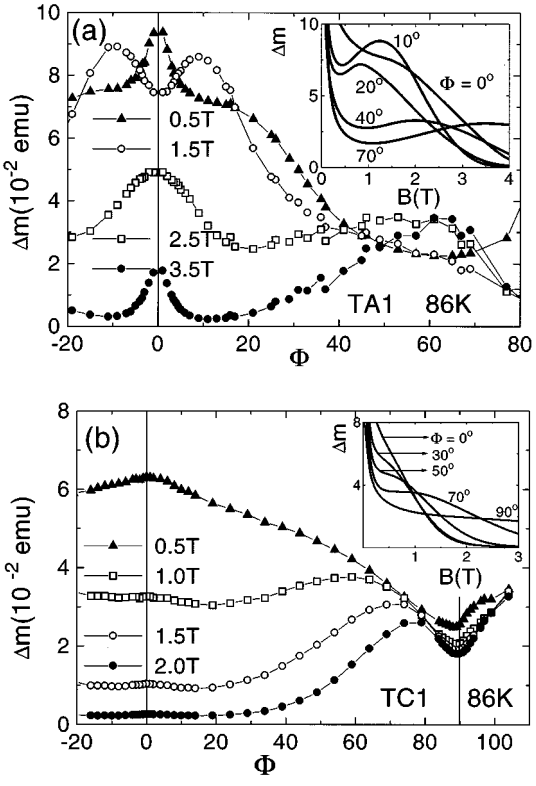

FIG. 13. Hysteresis width Δm vs angle Φ between applied magnetic field B and the c axis at different B values for the pure melt-textured Nd-123 sample TA1 (a) and the much less pure specimen TC1 (b). The inset in (a) shows the peak effect and the influence of the twin structure at $\Phi = 0°$, whereas in TC1 the peak is suppressed up to 70° and no influence of the twins is present [inset of (b)].

and from the twin structure. In Figs. 13(a) and 13(b) we show $\Delta m(\phi)$ at 86 K because in melt-textured material the influence of the twins decreases faster with decreasing temperature than in single crystals. The general difference between melt-textured and single crystalline specimens is the peak PE_{tw} caused by the twins which is only present in single crystals where the twin structure is of more importance. In the field region below PE [0.5 T in Fig. 13(a)] $\Delta m(\phi)$ shows a broad maximum from the residual large scale defects and within the trapping angle a pronounced peak at $\phi = 0$ from the correlated twin structure. At fields below 0.3 T this pinning from the twin walls becomes much less pronounced. In the peak regime [1.5 T in Fig. 13(a)] the dip in Δm within the trapping angle is caused by channeling or shearing of vortices along the twin walls as in single crystals. This behavior depresses at 86 K the peak at $\phi = 0°$ completely [inset of Fig. 13(a)], whereas at 77 K PE at $\phi = 0°$ is present (Fig. 12). In the field region above PE [2.5 and 3.5 T in Fig. 13(a)] twin wall pinning around $\phi = 0°$ dominates. The angular dependence of Δm at 3.5 T outside the trapping angle of about 15° is governed by the increase of B_{irr} with ϕ [inset in Fig. 13(a)].

Figure 13(b) shows $\Delta m(\phi)$ of sample TC1 with its negligible influence of twins. Only in the field region around 0.5 T [Fig. 13(b)] does residual pinning from the twins cause a small increase of Δm at $\phi = 0°$. The interaction from the large scale defects with the corresponding sharp decrease of $j(B)$ [inset in Fig. 13(b)] dominates below 0.5 T in the whole angular regime. The PE is absent just within this field region but it starts to develop outside, for instance, at 70° [inset of Fig. 13(b)]. This observation indicates that the necessary defect structure of clusters is present but the PE changes or is prevented from flux dynamics for the following reason. The origin of the PE is related to a transformation from a collective pinning interaction below the peak to a plastic deformation of vortices above which the shear modulus of the vortices softens and decreases towards B_{irr}.[20] The increase of the current with B results from a change of the transverse size R_c of the correlation volume. It decreases from a value much larger than the London penetration depth below B_p to a length comparable to the mean flux distance a_0 at the peak. However, strongly interacting defects cause plastic deformation and an amorphous vortex lattice with $R_c \approx a_0$. Therefore, in the field region where the large scale defects dominate, no collective interaction and, consequently, no minimum of j below B_p is expected. But if the concentration of large scale defects is low, a more regular vortex lattice may develop at larger fields above the pronounced $j(B)$ decrease. The field region where the large scale defects dominate is less dependent on ϕ [inset in Fig. 13(b)], whereas the field B_p at which the peak from the clusters appears scales with $B_{irr}(\phi)$, i.e., it increases with ϕ. If B_p is within or close to the field regime where the larger scale defects dominate no PE occurs. This is the case below about 50°. However, above 50°, B_p is shifted with increasing ϕ outside this field regime and a plateau in $j(B)$ as a precursor of a PE becomes visible. In summary, in order to realize a current minimum below B_p in the presence of strongly interacting second phase precipitates, it is necessary to move B_p sufficiently far away from their influence. This can be done by means of a high irreversibility field as realized with

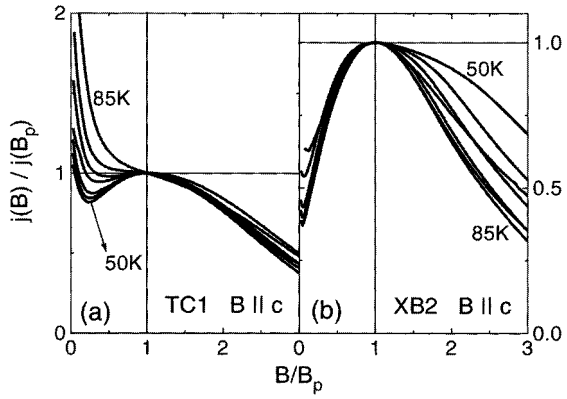

FIG. 14. Scaling behavior of the current density in the temperature region from 85 to 50 K. The current is normalized with its maximum value at the peak field B_p and the field is normalized with B_p. The less pure melt-textured sample TC1 shows a deviation from this scaling relation below B_p from the influence of the large scale defects (a), whereas the crystal XB2 shows less good scaling above B_p from the influence of the twins (b).

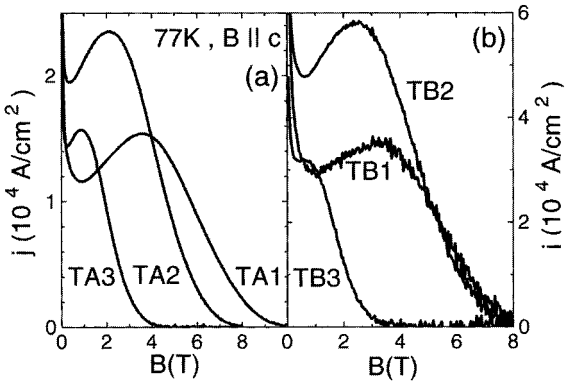

FIG. 15. Current density j vs B for two Nd-123 melt-textured specimens TA (a) and TB (b) after high-pressure oxydation (TA1 and TB1) and after two subsequent oxygen reduction steps 2 and 3.

sample TA1 and TB2 in Fig. 12. Naturally the formation of a current minimum is not desirable for optimizing j in the higher field region. But without the PE, large currents in this field regime around B_p are not obtainable by the large scale defect structure because B_{irr} is decreased to untolerably low values before the current at medium field is enhanced as shown for TC1. Therefore one needs the defect structure for the PE as well as, for higher currents at low fields, the strongly interacting defects. The concentration of both structures must be as low as is tolerable for the current in order to avoid a decrease of B_{irr}.

The indication that the defect structure—necessary for the PE—is also present in melt-textured materials is supported further by the same behavior of j with oxygen reduction. As shown in Tables I and II, oxygen deficiency results in melt-textured materials even in a lower T_c at the same condition of reduction as in single crystals. This clearly demonstrates that oxygen vacancies and the related clusters are present.

Figures 14(a) and 14(b) show the current density normalized to its maximum value at the peak field B_p vs B/B_p for the melt-textured sample TC1 and the single crystal XB2 at 85, 80, 75, 70, 65, 60, and 50 K. The nonscaling behavior of TC1 in Fig. 14(a) demonstrates the different temperature dependences of the clusters and the strongly interacting defects which become dominating at higher temperatures. At 85 K and above, their influence extends into the region of $B/B_p \approx 1$ which prevents the formation of the peak. However, with decreasing temperature the reduced field region where the large scale defects dominate is lowered and the PE starts to develop. For comparison, Fig. 14(b) shows the scaling in a single crystal with negligible strongly interacting defects. But here the PE becomes influenced by the twin structure and the scaling is therefore less perfect. This interference from channeling or shearing which results in a broadening of the peak at $B \| c$ from the dip in $\Delta m(\phi)$ at $\phi = 0°$ becomes more pronounced at lower temperatures. The most perfect scaling behavior is observed in single crystals with no twins or with a large concentration of clusters and pointlike defects depressing the influence of the twin structure.

The optimization of the current by means of oxygen reduction was also made in the melt-textured specimens. Increasing δ, starting from high-pressure oxidation, results qualitatively in the same dependences of T_c, B_{irr}, and j on δ as in single crystals. But the transition temperature and B_{irr} decreased faster in the melt-textured specimens deoxidized under the same condition as single crystals. For instance, T_c droped from 95.5 K in the high-pressure oxydized specimen (TA1, $\delta < 0.04$) to 90.6 K (TA3), whereas the T_c reduction in XA5 was only 0.7 K for the same oxygen treatment. The given δ values are related to the oxygen treatment and do not consider different diffusion kinetics of oxygen between single crystals and melt-textured specimens leading to different oxygen content after the same treatment. The maximum current is therefore not at $\delta = 0.09$ as for XA5 but at 0.05 as shown in Figs. 15(a) and 15(b) for specimen TA2 and TB2. Naturally the oxidation steps in Figs. 15(a) and 15(b) for the melt-textured material were too large in order to find the precise δ for the maximum current. But nevertheless the second step (TA3, TB3) which corresponds to the value at which the single crystal has its j maximum is clearly on the decreasing branch of $j(\delta)$. The same tendency was observed for the less pure single crystal (XB) shown in Fig. 7. There are three reasons for this different behavior of T_c, B_{irr}, and j between pure single crystals and much less pure melt-textured specimens. As mentioned before, the same oxygen treatment in single crystalline and melt-textured specimens does not lead to the same oxygen content. This can be deduced from the stronger T_c reduction in the melt-textured material. Secondly, the larger amount of defects in the melt-textured material may require to add a lower concentration of oxygen vacancies in order to obtain the maximum current. Finally, for the same reason—larger impurity content—the T_c reduction with increasing δ is expected to be stronger in melt-textured specimens. Summarizing, the optimization of the current in a less pure material by oxygen reduction is closer to the fully oxydized state. The development of the current in dependence on δ becomes influenced by the presence of the larger scale pinning centers which makes an improvement more difficult than in single crystals.

The irreversibility field in melt-textured materials and its dependence on the twin structure and the oxygen deficiency is qualitatively the same as in single crystals. Samples with a cusplike $B_{\mathrm{irr}}(\phi)$ dependence as TD1 show very high values

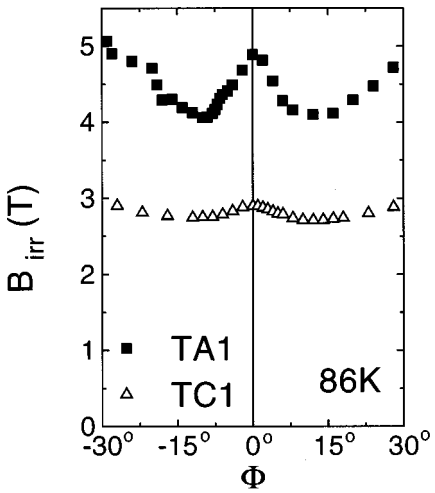

FIG. 16. Irreversibility field B_{irr} vs angle Φ between applied magnetic field B and the c axis for the pure Nd-123 melt-textured sample TA1 and the sample TC1 with much more impurities and second phases.

of up to 11.8 T at $\phi=0°$, 77 K because the uncorrelated defect structure does not influence the twin structure too much. This means that the highest values of B_{irr} are obtained in samples with low current densities as in single crystals. The large scale defects in the melt-textured material do not reduce T_c but they diminish the planarity of the twin structure and its capability to increase B_{irr}. This effect is demonstrated by the comparison of B_{irr} from sample TA1 and TC1 in Fig. 16. The cusplike behavior of $B_{irr}(\phi)$ is much less pronounced in specimen TC1 with the higher content of second phase particles. This different behavior was already discussed and shown in Figs. 13(a) and 13(b), where specimen TA1 exhibits twin wall pinning within the trapping angle quite in contrast to TC1. This additional interference of the strongly interacting uncorrelated defects makes an optimization of B_{irr} combined with a large current density more difficult than in single crystals. But there is also a positive influence of this defect structure on B_{irr} from the following observation. Specimen XA7 and TA1 exhibit about the same T_c values and very similar B_{irr} values for $B\|c$ at 86 K. However, the cusplike increase of B_{irr} from the Bose glass transition at $\phi=0°$ is in XA7 about 100% (Fig. 9), whereas it is only 20% in TA1 (Fig. 16), i.e., outside the trapping angle the $B_{irr}(\phi)$ value in the melt-textured material is considerably higher. This benefit from the strongly interacting defect structure is expected if the nature of B_{irr} changes towards a depinning like transition. Such a behavior is always observed when a large number of uncorrelated defects is introduced by fast neutron or proton irradiation. Therefore, B_{irr} in melt-textured samples is expected to show for an optimal uncorrelated large scale defect structure an increase outside the trapping angle as in TA1.

D. Relaxation behavior

Finally we discuss the normalized relaxation rate $S=d(\ln \Delta m)/d(\ln dB/dt)$ which was obtained from measuring magnetization with different sweep rates. Using Δm instead of the irreversible moment at the increasing or decreasing branch of the magnetization eliminates the influence of the reversible moment. But this method gives the mean value of the relaxation from both branches and is therefore not able to detect a possible asymmetric behavior for instance from a surface barrier. In order to check this we determined first the unnormalized relaxation rate $R=dm/d(\ln dB/dt)$ which is shown for specimens XA5, TA1, and TC1 in Fig. 17. The values $R(B)$ for increasing B ($R<0$) and decreasing B ($R>0$) show satisfying symmetry except at fields below 1 T. This results from demagnetization effects and is therefore more pronounced for the large sample sizes of the melt-textured materials. The measurements were made starting from a sufficiently large negative field in order to avoid problems with partial penetration of the vortex state. The field dependence of R is in all three specimens similar concerning the maximum value of R at about 0.5 B_{irr}. The increase of R at low fields in TA1 and especially in TC1 results from the larger scale defects.

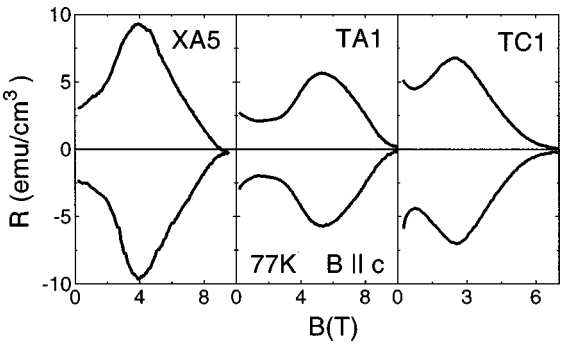

FIG. 17. Relaxation rates $R=dm/dln(dB/dt)$ vs applied magnetic field B for the Nd-123 single crystal XA5 and the melt-textured specimens TA1 and TC1.

The normalization of R is made using the equation above. The corresponding S values, shown in Fig. 18, are therefore slightly larger than those ones normalized by the value measured at the maximum sweep rate or obtained as usually from the time-dependent decay of m normalized by the value which is measured at the beginning of the decay. This difference becomes larger in the field region where S increases with B, i.e., above the plateau where S is about 0.05. The field dependence of S consists of this plateau which contains a shallow minimum followed by a roughly linear increase

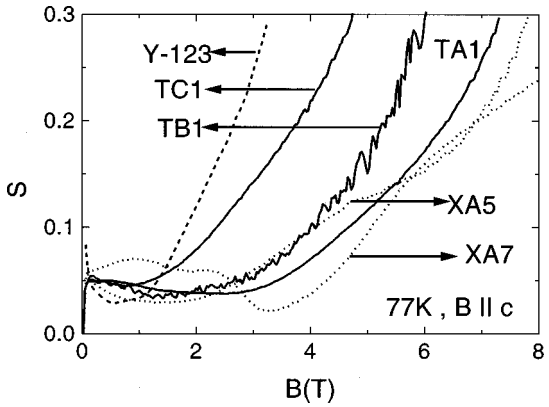

FIG. 18. Normalized relaxation rate $S=d\ \ln(\Delta m)/d\ \ln(dB/dt)$ vs applied magnetic field B for an Y-123 crystal, the Nd-123 crystal XA, and the melt-textured samples TA, TB, and TC. The field region with a tolerable low thermal relaxation of $S\leqslant 0.1$ becomes spread out with larger irreversibility fields.

with B which becomes steeper towards B_{irr}. This is the case for all S values shown in Fig. 18 except for the relaxation of XA7 which has a much more complicated field dependence due to the influence of the twin structure. In Ref. 19 it was shown that S increases in the field region where channeling or shearing of vortices becomes important, whereas it is reduced if pinning by twins dominate. Therefore the maximum of S in XA7 at 2.2 T and the minimum at 3.3 T maybe tentatively related to the first and second interaction, respectively.

The inverse value of S is equal to the exponent n if the $E(j)$ characteristics are approximated by a power-law relation $E \sim j^n$. A minimum n value of 10 may be related to the maximum tolerable losses for any application. Therefore the plateau of $S(B)$ with n of about 10 is the field region within which the $E(j)$ characteristics are sufficiently steep. This region is determined by the irreversibility field and extends typically up to values of $0.3B_{irr}$. In Y-123 this regime of sufficiently low relaxation reaches values of about 1.5 T (Fig. 18), whereas in Nd-123 3 to 4 T can be obtained.

IV. CONCLUSION

$NdBa_2Cu_3O_{7-\delta}$ single crystals and melt-textured samples have been prepared under low oxygen partial pressure from Nd poor starting mixtures. In this way the Nd/Ba substitution could be reduced to below its detection limit, and the Nd-422 phase content of the melt-textured samples could be limited to less than 10%. After proper oxidation the samples exhibited T_c values of up to 95.5 K.

The interference between correlated disorder in the flux lattice from twins and uncorrelated disorder from small clusters, and strongly interacting second phase particles was investigated. The pointlike disorder from oxygen vacancy clusters is responsible for the peak of the current density vs field. A second, but less pronounced peak of the current vs field could be related to the twin structure by angular-dependent measurements of the magnetic moment. In single crystals and melt-textured samples the current density is minimal after high-pressure oxidation and passes a maximum with decreasing oxygen content. This optimization of the current density at 77 K results in values of 1.2×10^5 A/cm^2 and 5.8×10^4 A/cm^2 at the peak at fields of 2.1 T for a single crystal and 2.5 T for a melt-textured sample, respectively. In both specimens the current is still above 4×10^4 A/cm^2 at 4 T, 77 K. In order to obtain such large currents at fields of 4 T, 77 K it is essential that the peak effect be present and that high irreversibility fields are maintained. In pure crystals and melt-textured samples with low currents, the irreversibility fields for $B\|c$ at 77 K reach 13.4 and 11.8 T, respectively. These extremely high values are caused by the twin structure; its corresponding cusplike maximum of B_{irr} at $B\|c$ decreases to moderate values outside the trapping angle. Introducing pointlike disorder by oxygen reduction or second phase particles destroys the correlated influence of the twins on the flux lattice and B_{irr} decreases. For this reason the irreversibility field in the current optimized crystals and melt-textured samples was reduced to 10 and 8 T at 77 K, respectively. This indirect influence of the twin structure via B_{irr} on the current in samples with an optimized current density is much larger than its direct influence via pinning or channeling. The relatively low content of strongly interacting second phase particles in the melt-textured specimens is still sufficient to increase the current at low fields. As long as this content is low the high level of B_{irr} from the twins is hardly affected and the peak of the current develops. On the other hand, B_{irr} becomes lower if the uncorrelated influence of these precipitates on the vortex lattice increases. In this case the field region of the peak decreases and starts to overlap with the region where the strongly interacting second phase particles dominate and the advantage of the peak is reduced.

ACKNOWLEDGMENTS

We appreciate many useful discussions with A. A. Zhukov and W. Jahn and we would like to thank A. Will for performing VSM measurements and D. Ernst for the x-ray analysis.

[1] M. Murakami, Supercond. Sci. Technol. **5**, 185 (1992).
[2] K. Salama and D. F. Lee, Supercond. Sci. Technol. **7**, 177 (1994).
[3] S. I. Yoo *et al.*, Jpn. J. Appl. Phys. **33**, L1000 (1994).
[4] Th. Wolf *et al.*, *Proceedings of the 8th International Workshop on Critical Currents* (World Scientific, Singapore, 1996), p. 411.
[5] Th. Wolf, J. Cryst. Growth **166**, 810 (1996).
[6] S. Takekawa *et al.*, Jpn. J. Appl. Phys. **26**, L2076 (1987).
[7] C. T. Lin *et al.*, Physica C **272**, 285 (1996).
[8] T. Wada *et al.*, Appl. Phys. Lett. **52**, 1989 (1988).
[9] J. L. Tallon and B.-E. Mellander, Science **258**, 781 (1992).
[10] S. I. Yoo *et al.*, IEEE Trans. Appl. Supercond. **5**, 1568 (1995).
[11] E. A. Goodilin *et al.*, Physica C **272**, 65 (1996).
[12] Th. Wolf (unpublished).
[13] H. Claus *et al.*, Physica C **200**, 271 (1992).
[14] Th. J. Kistenmacher, Solid State Commun. **65**, 981 (1988).
[15] G. V. M. Williams and J. L. Tallon, Physica C **258**, 41 (1996).
[16] Th. Wolf *et al.*, J. Cryst. Growth **96**, 1010 (1989).
[17] K. Kishio *et al.*, Mater. Res. Soc. Symp. Proc. **156**, 91 (1989).
[18] A. A. Zhukov *et al.* (unpublished).
[19] H. Küpfer *et al.*, Phys. Rev. B **54**, 644 (1996).
[20] H. Küpfer *et al.* (unpublished).
[21] A. Erb *et al.*, J. Low Temp. Phys **105**, 1023 (1996).
[22] G. Blatter *et al.*, Rev. Mod. Phys. **66**, 1125 (1994).
[23] K. Saito *et al.*, Czech. J. Phys. **46**, 1545 (1996).
[24] M. Murakami *et al.*, *Proceedings of the 8th International Workshop on Critical Currents* (Ref. 4), p. 57.
[25] M. R. Koblischka *et al.*, Phys. Rev. B **54**, R6893 (1996).
[26] A. J. J. van Dalen *et al.*, Supercond. Sci. Technol. **9**, 659 (1996).
[27] M. Oussena *et al.*, Phys. Rev. B **51**, 1389 (1995).
[28] A. A. Zhukov *et al.*, Phys. Rev. B **52**, R9871 (1995).
[29] W. K. Kwok *et al.*, Phys. Rev. Lett. **72**, 1092 (1994).
[30] D. S. Fisher *et al.*, Phys. Rev. B **43**, 130 (1991).
[31] D. R. Nelson and V. M. Vinokor, Phys. Rev. Lett. **68**, 2398 (1992).
[32] H. Küpfer *et al.*, Phys. Rev. B **52**, 7689 (1995).